

Dual Actuation for High Speed Atomic Force Microscopy

S. Kuiper* A.J. Fleming** G. Schitter*)***

* *Delft Center for Systems and Control, Precision and Microsystems Engineering, Delft University of Technology, Mekelweg 2, 2628CD, Delft, The Netherlands.*

** *School of Electrical Engineering and Computer Science, University of Newcastle, Callaghan, NSW 2308, Australia.*

*** *Automation and Control Institute, Vienna University of Technology, Gusshausstrasse 27-29, 1040 Vienna, Austria.
(e-mail: stefan.kuiper@tudelft.nl, andrew.fleming@newcastle.edu.au, schitter@acin.tuwien.ac.at)*

Abstract

In atomic force microscopy (AFM) the imaging speed is strongly limited by the bandwidth of the feedback loop that controls the interaction between the measurement tip and the sample. A significant increase in closed-loop bandwidth can be achieved by combining a long-range, low-bandwidth actuator with a short-range, high-bandwidth actuator, forming a dual actuated system. This contribution discusses the design of a model-based feedback controller that controls the tip-sample interaction in dual actuated AFM. In order to guarantee closed-loop stability, the dynamic uncertainties of the system are identified and taken into account in the controller design. Two different design cases are discussed, showing the trade-off between the positioning range at lower frequencies and the positioning range at higher frequencies. The designed feedback controller is implemented on the prototype AFM system and demonstrates a disturbance rejection bandwidth of 20 kHz.

Keywords: Atomic Force Microscopy, model-based control, piezoelectric actuator, dual actuation.

1. INTRODUCTION

Atomic Force Microscopes (AFM) are important tools in nanotechnology, providing images of sample topography with molecular resolution by probing the sample with a very sharp tip. One of the main limitations of AFM, however, is its relatively low imaging speed [Hansma et al. (2006)]. Recently, several advancements are made to increase the lateral scanning speed of these instruments by improved hardware design, and applying modern control techniques [Croft and Devasia (1999); Ando et al. (2001); Schitter et al. (2007)]. Nowadays, the main limitation on the imaging speed is considered to be the bandwidth of the vertical feedback loop that controls the separation between the measurement tip and sample. Several attempts are made to increase the bandwidth of this feedback loop by using modern model-based controller design techniques [Schitter et al. (2001); Salapaka et al. (2002); Sebastian and Salapaka (2005)], showing a significant improvement in closed loop bandwidth as compared to the classical PI-controllers used in many commercially available systems nowadays. The achievable closed-loop bandwidth of these systems is strongly limited by the actuator dynamics. Several prototype scanners are reported in literature with improved mechanical design, aiming to push the resonant frequencies of these actuators as high as possible [Knebel et al. (1997); Ando et al. (2001); Schitter et al. (2007)].

This increase in resonance frequencies of these actuators often comes to the price of a reduction in positioning range. The full positioning range, however, is most often only needed to track the relatively slow topography changes. A vast improvement on the closed loop bandwidth can therefore be achieved by combining a long-range, low-bandwidth actuator with a short-range, high-bandwidth actuator forming a dual actuated system. This technique has been successfully implemented on HD-drives [Mori et al. (1991); Horowitz et al. (2007)], and has also been demonstrated in prototype scanning probe microscopes [Mamin et al. (1994); Sulchek et al. (1999); Jeong et al. (2007); Schitter et al. (2008); Fleming (2009b)].

This contribution is focussed on designing a model-based feedback controller for a dual actuated AFM to achieve a closed loop bandwidth that is as high as possible. Special emphasis is hereby given on how to assign different frequency regions to the actuators, taking into account the frequency dependent positioning range and also robust stability of the controlled system. The used experimental setup is introduced in Section 2, and the design of the model-based feedback controller is discussed in Section 3. The achieved closed-loop disturbances rejection bandwidth is verified experimentally in Section 4.

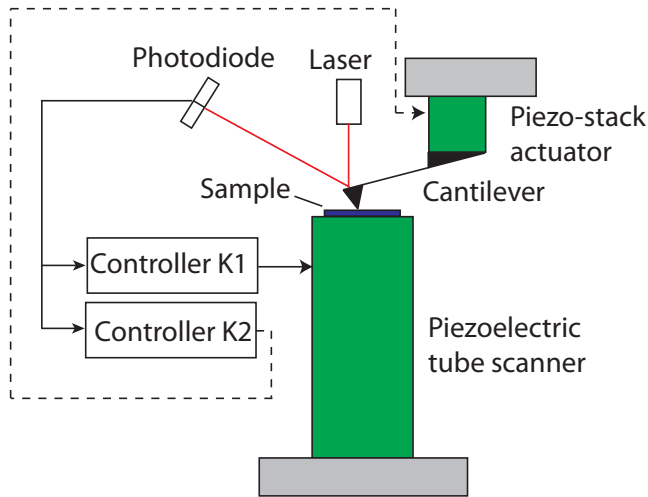


Figure 1. Schematic description of a dual actuated atomic force microscope.

2. SYSTEM DESCRIPTION

A schematic description of the system is shown in Figure 1. The sample is placed on a commercially available tube scanner (J-scanner, Veeco, Santa Barbara, USA), which provides the scanning motion of the sample during imaging, as well as the long-range vertical positioning of the sample to control the tip-sample interaction with a maximum range of $5 \mu\text{m}$. The tip-sample force is measured by reflecting a laser beam off the free end of the micro cantilever where the measurement tip is mounted at, and measuring the deflected laser spot with a segmented photodiode. This system is extended to a dual actuated system by using a small piezoelectric plate actuator (CMAP12, Noliac, Kvistgaard, Denmark) which is glued onto the cantilever holder to form the new mounting spot for the cantilever-chip (cf. Fig. 1), and allows vertical positioning of the cantilever-chip with a maximum range of about $0.5 \mu\text{m}$. Due to its high stiffness, and low-mass the piezoelectric plate actuator is capable of actuating the cantilever chip at very high bandwidth. However, to drive this piezoelectric plate actuator at the required bandwidth, a special amplifier is required to cope with the relatively large capacitive load of 36 nF .

2.1 Electrical Considerations

The foremost bandwidth limitations of a high-voltage amplifier are the small-signal bandwidth, output-impedance, cable inductance, and power dissipation [Fleming (2009a)]. When driving a capacitive load of 36 nF with a typical amplifier having an output impedance of 10Ω , the small signal bandwidth would be limited to 44 kHz . Although a number of wide bandwidth high-voltage amplifier designs have been published [Müller (2005); Müller et al. (2006)], these are designed for electro-optic modulators with capacitances on the order of 100 pF . To overcome the bandwidth limitations associated with a large capacitive load, the high-speed *dual-amplifier* shown in Figure 2 is utilized [Fleming (2009a)]. The dual-amplifier consists of a standard high-voltage amplifier combined with a fast low-voltage stage to improve performance at higher frequen-

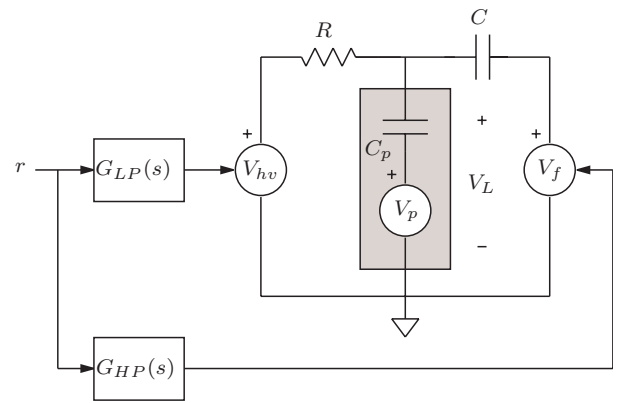


Figure 2. High-speed dual-amplifier Fleming (2009a). The reference signal r is applied simultaneously to a slow high-voltage amplifier V_{hv} and a fast low-voltage amplifier V_f . The two amplifiers are coupled to the load through R and C respectively.

cies. This arrangement has been demonstrated to successfully drive a 100 nF capacitance with a 300-kHz 20-Vp-p sine wave with negligible phase delay and a peak-to-peak current of 3.8 A [Fleming (2009a)]. With a voltage range of 200 V and peak current of 1.9 A , a standard amplifier would require a worst-case power dissipation of 380 W . However, the dual-amplifier arrangement has a worst-case power dissipation of only 30 W . As the Noliac CMAP12 actuator presents a load capacitance of only 36 nF , the dual-amplifier provides a small-signal bandwidth of greater than 2 MHz and a power-bandwidth of 800 kHz ($V_o=20 \text{ Vp-p}$).

2.2 System identification

To capture the system dynamics, the frequency responses from the amplifier inputs towards the cantilever deflection signal are measured using a network analyzer (4395A, Agilent, Santa Clara, USA). To also capture the dynamic uncertainties under working conditions, the measurements are repeated in several runs using different combinations of samples and cantilevers. Figure 3 (dashed) shows the results of two typical measurement runs for both actuators, revealing the first resonant mode of the tube scanner at 8 kHz and the first resonant mode of the piezoelectric plate actuator at 150 kHz . Based on averaged measurement data of 12 different measurement runs, two 7th order transfer functions are fitted to model the nominal dynamics of the individual actuators, as shown in Figure 3 (dashed-dotted). Based on the measurement data of the various measurement runs and the dynamical models, the maximum multiplicative uncertainty is determined at each frequency point, shown Figure 3 (solid). The models of the nominal actuator dynamics are used to design the model-based feedback controller, while the multiplicative uncertainty data is used to analyze the stability robustness of the closed loop system under working conditions.

3. CONTROLLER DESIGN

To minimize the force variations between the tip and sample, and to provide a good estimate of the sample topography during AFM imaging, a feedback controller should be designed with the following properties:

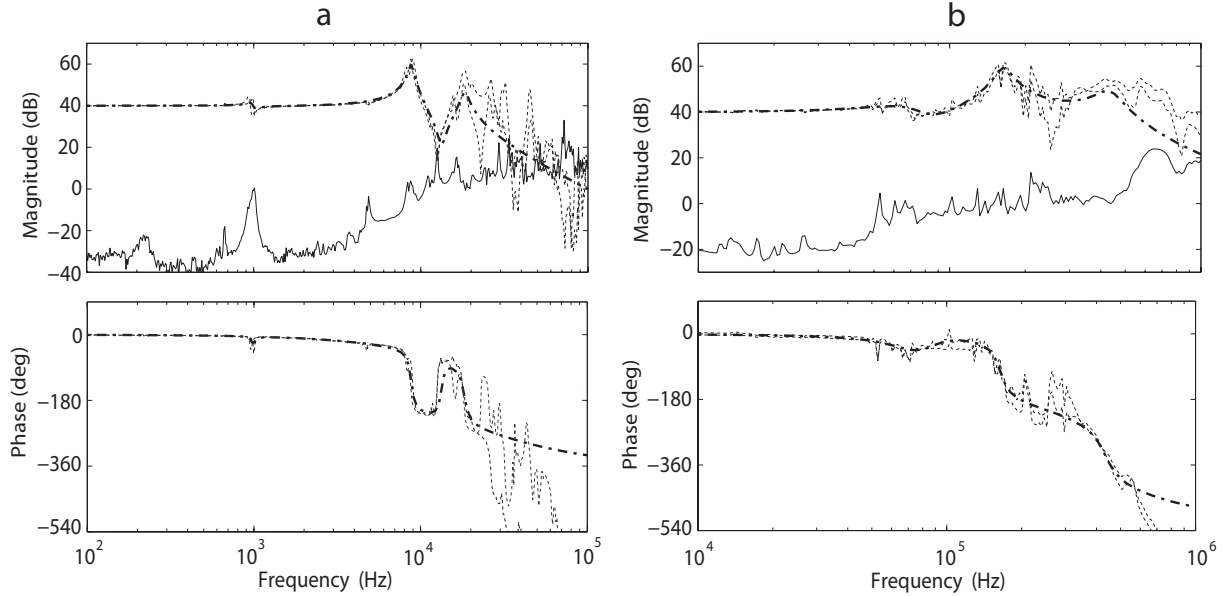


Figure 3. Frequency responses from the tube scanner (a) and of the plate actuator (b), for two different measurement runs (dashed), the 7th order model capturing the nominal dynamics (dashed-dotted), and the maximum multiplicative uncertainty (solid).

- Provide a disturbance rejection bandwidth which is as high as possible
- Make optimal use of the actuators positioning ranges
- Provide robust stability against dynamic uncertainties

The disturbance spectrum to be tracked by the vertical feedback loop in AFM, can be split into components stemming from the actual sample topography, and components stemming from a possible tilt of the sample. In most cases the variation of the sample topography is relatively small as compared to the width of the sample. Therefore, the larger height variations are mainly caused by a tilt of the sample. Consequently, the disturbance signal has a predominantly triangular shape with a base frequency equal to the line-scan frequency, and an amplitude spectrum which decays inversely proportional to the frequency. The underlying assumption of dual actuation is that the long-range actuator primarily tracks the larger amplitude, low-frequency height variations (such as from the sample tilt) and the short-range actuator has sufficient range to track the high-frequency topography variations. To prevent saturation of the short-range actuator the feedback controller should provide a frequency separation, assigning the low-frequency height variations to the long-stroke actuator, and the high-frequency height variations to the short-range actuator. The feedback controller design taking into account the frequency separation is performed by using model-based controller design methods [Skogestad and Postlethwaite (2005)].

3.1 Model-based feedback controller design

Figure 4 shows the block diagram of the system representation used for model-based controller synthesis, with the actuator dynamics $G(s) = \text{diag}[G_1(s), G_2(s)]$, weighting filters $W_e(s)$, $W_y(s) = \text{diag}[W_{y1}(s), W_{y2}(s)]$, and $W_u(s) = \text{diag}[W_{u1}(s), W_{u2}(s)]$, and the to be designed

controller $K(s, \theta) = [K_1(s, \theta), K_2(s, \theta)]^T$, where indices 1 and 2 refer to the long-range actuator and the short-range actuator, respectively. The goal of the controller synthesis is to find controller parameters θ that minimizes the H_∞ -norm of the transfer from disturbance $d(t)$ towards the outputs of the weighting filters $[z_1(t) \bar{z}_2(t) \bar{z}_3(t)]^T$ (cf. Fig. 4), i.e. the controller $K(s, \hat{\theta})$ which renders,

$$\gamma \geq \min_{\theta} \left\| \begin{array}{c} W_e(s) \cdot S(s, \theta) \\ W_y(s) \cdot T(s, \theta) \\ W_u(s) \cdot S(s, \theta) \cdot K(s, \theta) \end{array} \right\|_{\infty}, \quad (1)$$

with $S(s, \theta) = (1 + [G_1(s), G_2(s)] \cdot K(s, \theta))^{-1}$ the sensitivity function, and the transfer towards the individual actuators outputs $T(s, \theta) = G(s) \cdot K(s, \theta) \cdot S(s, \theta)$.

The desired frequency responses of the closed-loop system can be enforced by setting the inverse frequency response behavior to the corresponding weighting filters. The transfer from the disturbance $d(t)$ towards the control error $e(t)$ (cf. Fig. 3.4) should be made as small as possible up to a certain frequency, which can be enforced in the controller synthesis by choosing weight $W_e(s)$ as an inverse high-pass filter. The disturbance rejection bandwidth that can be achieved is limited by the dynamical uncertainties of the actuator responses which are becoming larger for increasing frequency (cf. Fig. 3). To guarantee closed-loop stability a roll-off must be provided by the controller in order to attenuate these dynamical uncertainties, which for the long-range actuator is found to be necessary at a corner frequency of 6 kHz, and for the short-range actuator at a corner frequency of 40 kHz. This roll-off can be enforced in the controller synthesis by the choosing weighting filters $W_{y1}(s)$ and $W_{y2}(s)$ as inverse low-pass filters with the corresponding corner frequencies. Critical in the design of a feedback controller for dual actuated systems is the frequency region where the short-range actuator takes over from the long-range actuator [Schroek and Messner (1999)]. The transition between both actuators in this

frequency region is strongly determined by the required roll-off for the long-range actuator, and the chosen roll-on frequency for the short-range actuator. The roll-on for the short-range actuator can be enforced by choosing the weight $W_{u2}(s)$ as an inverse band-pass filter:

$$W_{u2}^{-1}(s) = \alpha \cdot \underbrace{\frac{s + 2\pi}{s + 2\pi \cdot \omega_c}}_{\text{high-pass}} \cdot \underbrace{\frac{s + 2\pi \cdot 4 \cdot 10^6}{s + 2\pi \cdot 4 \cdot 10^4}}_{\text{low-pass}}, \quad (2)$$

where ω_c determines the corner frequency of the high-pass behavior, and gain α determines the allowable peaking of the control action for the short-range actuator. The roll-on frequency ω_c should not be chosen too close to the roll-off frequency of the long-range actuator, as this might result in a too fast transition between both actuators, leading to a large phase difference between both control paths. If in the cross-over region the phase differences between both control paths exceeds 120° , the actuators will start to compensate part of each others motion in that frequency region [Schroeck and Messner (1999)]. This can result in a peaking of the short-range actuators control action in the cross-over region, and therefore a reduction of the positioning range at those frequencies. A too low roll-on frequency for the short-range actuator, however, might compromise the positioning range at lower frequencies.

3.2 Synthesis results

To demonstrate the design trade-off between the positioning range at lower frequencies and the positioning range at higher frequencies for dual actuated systems, two design cases are discussed using different parameters for the weight on the control action for the short-range actuator of Equation 2. The first design is aimed for a lower cross-over frequency between both actuators, but with minimal peaking of the control action for the short-range actuator, by choosing $\omega_c = 500$ Hz, and $\alpha = 1$. The second design is aimed for a higher cross-over frequency between both actuators, thereby allowing some peaking of the control action of the short-range actuator by choosing $\omega_c = 2$ kHz, and $\alpha = 3/2$. The choices for the other weighting filters are kept equal for both designs and are given in Table 3.2. The controller synthesis is performed using the Robust Control Toolbox of `matlab`, which in both cases results in $\gamma \geq 2.9$, meaning that the resulting closed-loop systems are close to the design goals governed by the weighting filters. Figure 5 shows the contributions of both the long-range actuator and the short-range actuator and the resulting complementary sensitivity functions for both design cases, showing that in both cases a complementary sensitivity bandwidth is achieved of 40 kHz. To analyze whether the resulting closed-loop systems are robustly stable, μ -analysis is performed using the identified multiplicative dynamic uncertainty (Fig. 3). The results are shown in Figure 6, showing that in both cases the μ -value is smaller than one for all frequencies. It can therefore be concluded that in both cases the closed loop system is robustly stable, i.e. sufficient attenuation of the uncertain dynamics is provided.

The difference between the resulting closed loop systems from both design cases is that in the first case the cross-over frequency between both actuators is at 550 Hz, and the peak gain of the short-range actuator is 0.7 dB (Fig.

Weight	Filter type	Corner frequency	Peak gain
$W_e^{-1}(s)$	High-pass	$\omega_e = 90$ -kHz	$\alpha_e = 2$
$W_{y1}^{-1}(s)$	Low-pass	$\omega_{y1} = 6$ -kHz	$\alpha_{y1} = 1$
$W_{y2}^{-1}(s)$	Low-pass	$\omega_{y2} = 40$ -kHz	$\alpha_{y2} = 1$
$W_{u1}^{-1}(s)$	Low-pass	$\omega_{u1} = 6$ -kHz	$\alpha_{u1} = 1$
$W_{u2}^{-1}(s)$	Band-pass	$\omega_c = [0.5, 3.5]$ -kHz $\omega_u = 40$ -kHz	$\alpha_{u2} = [1, (2/3)]$

Table 1. Choice of weighting filters for the model-based design of the feedback controllers

5a), whereas in the second design case the cross-over frequency is at 2 kHz, and the peak gain of the short-range actuator is 2 dB (Fig. 5b). These differences becomes more clear by comparing the frequency dependent positioning ranges of both systems.

3.3 Range comparison

The frequency dependent positioning range of the dual actuated system can be calculated by determining the gain at which one of the control paths saturates:

$$R(\omega) = \|T(i\omega)\| \cdot \beta(\omega), \quad (3)$$

with

$$\beta(\omega) = \min \left[\frac{r_1}{|S(i\omega) \cdot K_1(i\omega)|}, \frac{r_2}{|S(i\omega) \cdot K_2(i\omega)|} \right], \quad (4)$$

where r_1 , and r_2 are the maximum input ranges for the long-range and short-range actuator respectively. Figure 7 shows the calculated positioning ranges, showing that with the first design case the positioning range starts to roll off at a frequency of 50 Hz and for the second design case the positioning range starts to roll of at 150 Hz. The minimum positioning range, on the other side, is $0.46 \mu\text{m}$ at a frequency of 3.4 kHz for the first design case and $0.4 \mu\text{m}$ at a frequency of 6.5 kHz for the second design case. The dashed lines in Figure 7 indicate typical spectra for triangular disturbance signals, which indicate that when scanning a relatively flat but titled sample, the maximum line scan-speed is three times higher for the second design case with the higher cross-over frequency. This, however, comes at the cost of maximally 15% less positioning range in the frequency region between 3 to 10 kHz. The remaining $0.4 \mu\text{m}$ positioning range in that frequency region, however, is considered to be sufficient to track the sample topography. Therefore, for the rest of the text only the second design case with the higher cross-over frequency will be considered.

3.4 Controller reduction and implementation

The resulting feedback controller from the model based controller synthesis is a 19th order one input/two outputs (SITO) system. In order to facilitate implementation of the controller and to allow easy adjustment of the loop-gain when changing cantilevers, the controller is split in one common integrating action for both actuators and two separate SISO controllers denoted $\hat{K}_1(s)$ and $\hat{K}_2(s)$, as shown in Figure 8. The frequency response plots of these SISO controllers are shown in Figure 9, showing the notch filters to compensate for the individual resonant modes of the actuators and also the low-pass behavior

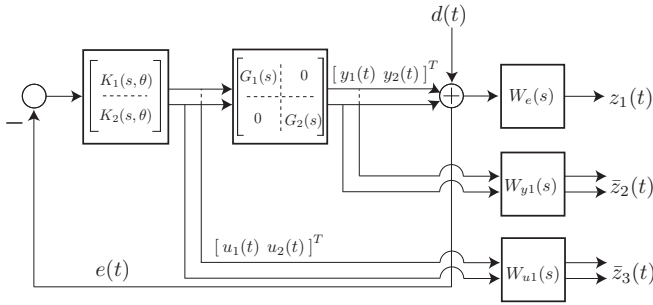


Figure 4. Block diagram of the system representation used for controller synthesis, with controller $K(s, \theta)$, plant dynamics $G(s)$, and weighting filters $W_e(s)$, $W_y(s)$, and $W_u(s)$.

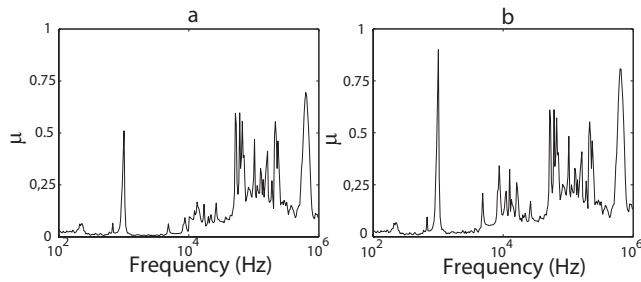


Figure 6. μ -plot for the closed loop system with low cross-over frequency between both actuators(a), and for closed loop system with high cross-over frequency, showing that in both cases the system is robustly stable for the dynamic uncertainties.

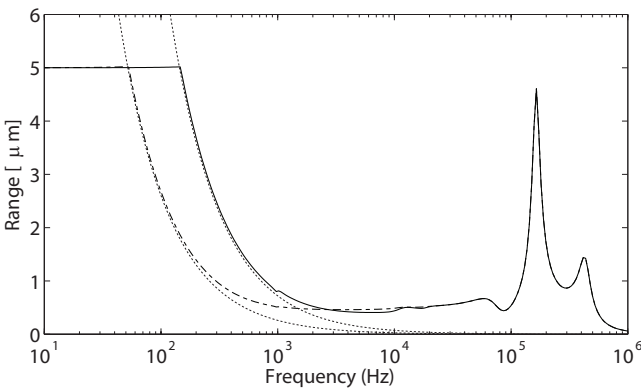


Figure 7. Vertical positioning range $[\mu m]$ as a function of frequency for the system with a low cross-over frequency (dash-dotted), and for the system with a high cross-over frequency (solid). The dashed lines indicate typical $1/\omega$ disturbance spectra.

in $\hat{K}_1(s)$ and high-pass behavior in $\hat{K}_2(s)$ to create the frequency separation between both actuators. To facilitate implementation of the controllers on the available signal processing hardware, the order of $\hat{K}_1(s)$ and $\hat{K}_2(s)$ are reduced to 7th and 8th order, respectively. The frequency responses of the reduced SISO controllers are shown in Figure 9 (dashed), showing only small deviations from the full-order controllers. The reduced SISO controllers are implemented on *Field programmable Analog Arrays* (FPAA), similar as presented in [Schitter and Phan (2008)].

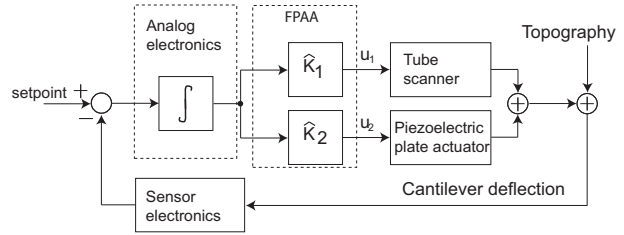


Figure 8. Block diagram of the dual actuated AFM.

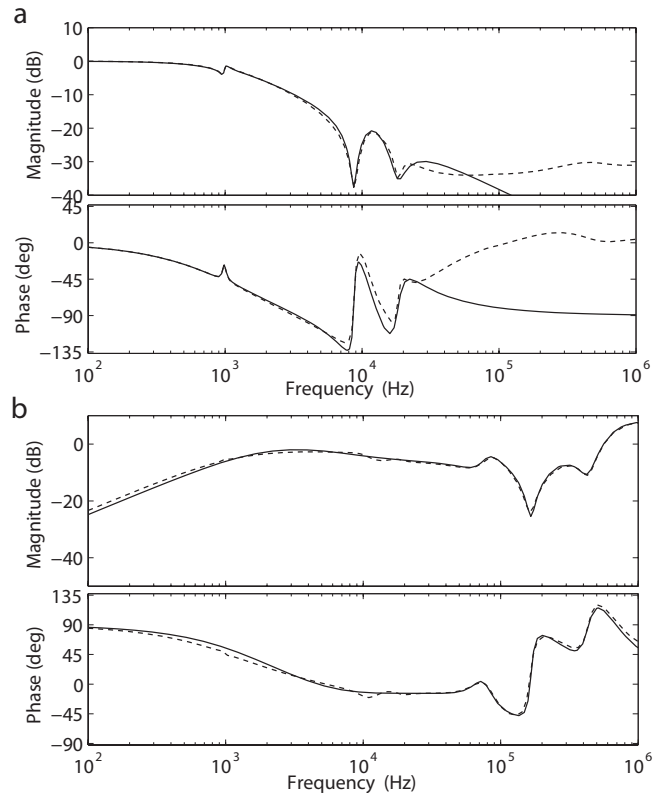


Figure 9. Bode magnitude plots of the controllers $\hat{K}_1(s)$ (a) and $\hat{K}_2(s)$ (b), full order (solid) and after model reduction (dashed).

4. EXPERIMENTAL RESULTS

In order to analyze the achieved disturbance rejection of the new dual actuated system, the sensitivity function of the prototype system is measured using a network analyzer (4395A, Agilent, Palo Alto, USA). The results are shown in Figure 10 (solid) together with the modeled sensitivity function (dashed), showing an achieved disturbance rejection bandwidth of 20 kHz. The measured sensitivity function deviates from the modeled sensitivity function due to some un-modeled resonant modes at 1 kHz and 50 kHz (Fig. 10). The closed loop system is found to remain stable under all working conditions. The achieved closed loop bandwidth is significantly higher than what can be achieved with the conventional single actuated system, resulting in reduced force variations while imaging.

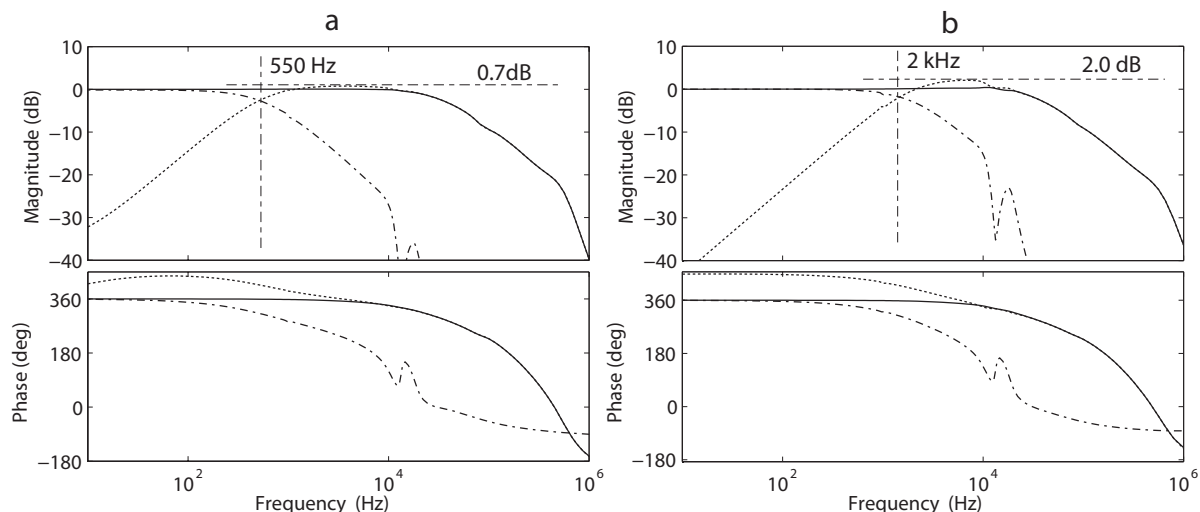


Figure 5. Frequency response plots of the complementary sensitivity function (solid) and the contribution of the low-bandwidth actuator (dashed-dotted), and the high bandwidth actuator (dashed) for the system with a controller designed for a low cross-over frequency between both actuators (a), and one for a higher cross-over frequency between both actuators (b).

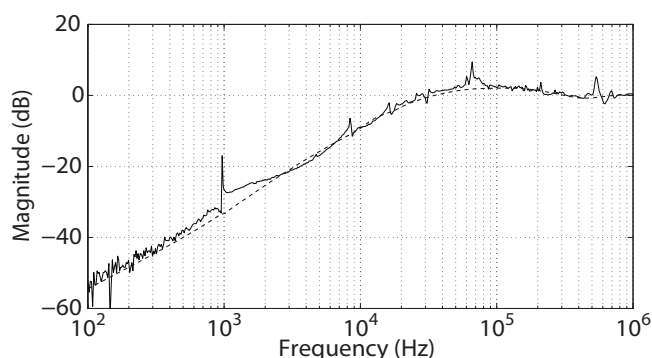


Figure 10. Frequency response of the measured (solid) and modeled (dashed) sensitivity function.

5. CONCLUSIONS

This contribution presents the design and implementation of a model-based feedback controller for a dual actuated AFM. Special emphasis is given on achieving a good frequency separation between both actuators, while also providing sufficient attenuation of the dynamic uncertainty to achieve robust stability under all working conditions. Two different model-based controllers are designed with different cross-over frequencies between both actuators, showing the trade-off between the positioning range at lower frequencies, and the positioning range at higher frequencies. The designed controller with one input and two outputs is split in one common integrating action, and two separate SISO controllers for both individual actuators, which are implemented on *Field Programmable Analog Arrays*. The resulting prototype system achieves a closed-loop disturbance rejection bandwidth of about 20 kHz. This disturbance rejection bandwidth is significantly higher than what can be achieved with the conventional system, which results in a reduction of variations of the imaging force while scanning and therefore allows for faster imaging.

ACKNOWLEDGEMENTS

The authors would like to thank C.J. Slinkman and A.P. van Dijke of the Delft Center for Systems and Control for their electronic support.

REFERENCES

- Ando, T., Kodera, N., Takai, E., Maruyama, D., Saito, K., and Toda, A. (2001). A high-speed atomic force microscope for studying biological macromolecules. *Proc. Nat. Acad. Sci.*, 98(22), 12468–12472.
- Croft, D. and Devasia, S. (1999). Vibration compensation for high speed scanning tunneling microscopy. *Rev. Sci. Instrum.*, 70, 4600–4605.
- Fleming, A.J. (2009a). A MHz bandwidth dual-amplifier for driving piezoelectric actuators and other highly capacitive loads. *Rev. Sci. Instrum.*, 80, 104701(1–7).
- Fleming, A. (2009b). High-speed vertical positioning for contact-mode atomic force microscopy. In *Proc. IEEE/ASME Intern. Conf. Adv. Intell. Mechatronics*, 522–527. Singapore.
- Hansma, P., Schitter, G., Fantner, G., and Prater, C. (2006). High speed atomic force microscopy. *Science*, 314, 601–602.
- Horowitz, R., Li, Y., Oldham, K., Kon, S., and Huang, X. (2007). Dual-stage servo systems and vibration compensation in computer hard disk drives. *Control Engin. Prac.*, 15(3), 291–305.
- Jeong, Y., Jayanth, G., and Menq, C. (2007). Control of tip-to-sample distance in atomic force microscopy: A dual-actuator tip-motion control scheme. *Rev. Sci. Instrum.*, 78, 093706(1–7).
- Knebel, D., Amrein, M., Voigt, K., and Reichelt, R. (1997). A fast and versatile scan unit for scanning force microscopy. *Scanning*, 19(4), 264–268.
- Mamin, H., Birk, H., Wimmer, P., and Rugar, D. (1994). High-speed scanning tunneling microscopy: Principles and applications. *J. Appl. Phys.*, 75, 161–186.

- Mori, K., Munemoto, T., Otsuki, H., Yamaguchi, Y., and Akagi, K. (1991). A dual-stage magnetic disk drive actuator using a piezoelectric device for a high track density. *IEEE Trans. Magnetics*, 27(6 Part 2), 5298–5300.
- Müller, H. (2005). Fast high-voltage amplifiers for driving electro-optic modulators. *Rev. Sci. Instrum.*, 76, 084701(1–7).
- Müller, H., Chiow, S., Long, Q., and Chu, S. (2006). Phase-locked, low-noise, frequency agile titanium:sapphire lasers for simultaneous atom interferometers. *Opt. Lett.*, 31(2), 202–204.
- Salapaka, S., Sebastian, A., Cleveland, J., and Salapaka, M. (2002). High bandwidth nano-positioner: A robust control approach. *Rev. Sci. Instrum.*, 73, 3232–3241.
- Schitter, G., Aström, K., DeMartini, B., Thurner, P., Turner, K., and Hansma, P. (2007). Design and modeling of a high-speed afm-scanner. *IEEE Trans. Control Syst. Technol.*, 15, 906–915.
- Schitter, G., Menold, P., Knapp, H., Allgöwer, F., and Stemmer, A. (2001). High performance feedback for fast scanning atomic force microscopes. *Rev. Sci. Instrum.*, 72, 3320.
- Schitter, G. and Phan, N. (2008). Field Programmable Analog Array (FPAA) based control of an Atomic Force Microscope. In *Proc. Am. Control Conf., 2008*, 2690–2695.
- Schitter, G., Rijkee, W., and Phan, N. (2008). Dual actuation for high-bandwidth nan positioning. In *Proc. 47th IEEE Conf. Decis. Control, 2008.*, 5176–5181.
- Schroeck, S. and Messner, W. (1999). On controller design for linear time-invariant dual-input single-output systems. In *Proc. Am. Control Conf., 1999.*, volume 6.
- Sebastian, A. and Salapaka, S. (2005). Design methodologies for robust nano-positioning. *IEEE Trans. Control Syst. Technol.*, 13(6), 868–876.
- Skogestad, S. and Postlethwaite, I. (2005). *Multivariable feedback control: analysis and design*. John Wiley & Sons.
- Sulchek, T., Minne, S., Adams, J., Fletcher, D., Atalar, A., Quate, C., and Adderton, D. (1999). Dual integrated actuators for extended range high speed atomic force microscopy. *Appl. Phys. Lett.*, 75, 1637–1639.